Title

Interplay between Cation and Anion Redox in Ni-Based Disordered Rocksalt Cathodes

Journal

ACS Nano, 15(8)

ISSN

1936-0851

Authors

Yue, Yuan
Ha, Yang
Huang, Tzu-Yang
et al.

Publication Date

2021-08-24

DOI

10.1021/acsnano.1c03289

Peer reviewed

Interplay between Cation and Anion Redox in Ni-Based Disordered Rocksalt Cathodes

Yuan Yue,[1‡] Yang Ha,[2‡] Tzu-Yang Huang,[1, 3] Ning Li,[1] Linze Li,[4] Qingtian Li,[2] Jun Feng,[2] Chongmin Wang,[4] Bryan D. McCloskey,[1, 3] Wanli Yang,[2*] and Wei Tong[1*]

[1] *Energy Storage and Distributed Resources Division, Lawrence Berkeley National Laboratory, Berkeley, CA 94720 USA*

[2] *Advanced Light Source, Lawrence Berkeley National Laboratory, Berkeley, CA 94720 USA*

[3] *Department of Chemical and Biomolecular Engineering, University of California, Berkeley, CA 94720, USA*

[4] *Environmental Molecular Sciences Laboratory, Pacific Northwest National Laboratory, Richland, Washington, 99352 USA*

Correspondence: wlyang@lbl.gov, weitong@lbl.gov

SUMMARY

The reversibility of the redox processes plays a crucial role in the electrochemical performance of lithium-excess cation-disordered rocksalt (DRX) cathodes. Here, we report a comprehensive analysis of the redox reactions in a representative Ni-based DRX cathode. The aim of this work is to elucidate the roles of multiple cations and anions in the charge compensation mechanism that is ultimately linked to the unique electrochemical performance of Ni-based DRX cathode. The low-voltage reduction reaction results in the low energy efficiency and strong voltage hysteresis. Our data reveal that the Mo migration between octahedral and tetrahedral sites enhances the O reduction potential, thus offering a potential strategy to improve energy

efficiency. This work highlights the important role that the electrochemically inactive transition metal plays in the redox chemistry and provides useful insights into the potential pathway to further address the challenges in Ni-based DRX systems.

KEYWORDS

Li-ion batteries, cathode materials, Li-rich transition metal oxides, cation-disordered rocksalt, Ni redox, oxygen redox, cation migration

INTRODUCTION

Continuous search of high-performance electrode materials to meet the increasing energy density demand for the Li-ion batteries has led to the development of several classes of cathodes over the decades.[1-3] Most of these materials – such as layered oxides and spinel – possess a well-ordered structure. In contrast, materials with cation-disordered structure were largely discarded until the electrochemical activity of the Li-excess cation disordered rocksalt (DRX) cathodes was demonstrated by Lee *et al.* in 2014.[4] The fundamental mechanism of the ion transport in the DRX cathodes is that the Li^+ hopping from one octahedral site to another octahedral site via an intermediate tetrahedral site (*o-t-o* diffusion).[4, 5] This percolation theory builds the foundation for this new class of high-capacity DRX cathodes.[4, 6]

Since then, a number of new DRX compounds with an exceptionally high capacity of 250 – 300 mAh g^{-1} have been successfully developed.[6] This large capacity is often achieved through the combined cationic transition metal (TM) and anionic O redox by tuning the accessible Li[7, 8] and TM redox center[9-19] via the high-valence TM charge compensation and/or bulk fluorination.[20-22] Ni is principally an attractive redox center for the design of DRX cathodes owing to the following three advantages: (1) high theoretical capacity associated with Ni^{2+}/Ni^{4+} double redox;

[10, 23] (2) relatively high operating potential of Ni^{2+}/Ni^{4+} redox;[24] and (3) facile synthesis of Ni^{2+}-based DRX materials in air.[25] However, these desired electrochemical attributes have yet to be fully achieved in the Ni^{2+}-based DRX systems. In contrast, the Ni-based DRX cathodes often exhibit the following characteristics: (1) incomplete Ni oxidation with the final oxidation state around 3+, though a high charge capacity is obtained with the complementary O oxidation;[25-27] (2) strong voltage hysteresis at the low-voltage plateau (~2 V) upon high-voltage cycling.[28-32] These features are manifested by a comparable charge energy density but lower discharge energy density, making the Ni redox center less favorable compared to other analogues (e.g., Mn).[11, 17, 22, 33-35] This phenomenon has been attributed to the slow Li^+ diffusion at the densified surface resulting from the oxygen evolution during charge and different redox potential for anionic oxygen due to the small charge transfer band gap of the oxidized Ni^{3+} in DRX systems.[26] There have been previous reports showing the incorporation of high-valence TM[30, 36] and fluorine substitution[18, 28] can address the challenge in poor energy efficiency to some extent. However, the underlying mechanisms regarding their roles in manipulating the redox mechanism and potential interplay during electrochemical cycling have not been well understood, which is essential to devise effective strategies to further improve the Ni-based DRXs.

In this work, we report a comprehensive analysis of both the cationic and anionic redox reactions in $Li_{1.15}Ni_{0.45}Ti_{0.3}Mo_{0.1}O_{1.85}F_{0.15}$ (LNTMOF), a representative Ni^{2+}-based DRX compound with a minimal low-voltage plateau reported so far. Specifically, the cationic Ni and anionic O redox reactions during charge and discharge have been carefully examined using combined electroanalytical and spectroscopic techniques. Ni-based DRXs exhibit the voltage hysteresis at the lower voltages than those Mn-based analogs. Compared to the Mo-free Ni-Ti DRX,

$Li_{1.15}Ni_{0.35}Ti_{0.5}O_{1.85}F_{0.15}$ (LNTOF), we provide further evidence of the roles of the redox processes and their interplay in the LNTMOF cathode with three cations and two anions that all strongly influence the overall redox processes. The most remarkable finding is the Mo migration between octahedral and tetrahedral sites during charge and discharge that appears to promote the potential of O reduction reaction. This work unravels a new understanding on the role of the electrochemically inactive Mo on the O redox behavior in Ni-based DRX material and sheds lights on the potential pathway to alleviate the large hysteresis for the further advancement of new DRX cathodes.

RESULTS AND DISCUSSION

LNTMOF Synthesis and Electrochemistry

Synthesis of LNTMOF samples is first investigated at the annealing temperature of 700 and 800 °C, both leading to a pure rocksalt phase (**Figure 1a**).[37] Using Debye – Scherrer equation, the crystallite size is determined to be ~30 and 53 nm for the LNTMOF sample annealed at 700 and 800 °C, respectively. Consistently, the secondary particle size also increases with annealing temperature (**Figure 1b, c** & **Figure S1-2**). The local structure of both samples is further investigated by scanning transmission electron microscopy (STEM) at the atomic level. Again, the cubic rocksalt structure is confirmed by the high-angle annular dark-field STEM (HAADF-STEM) images (**Figure 1d, e**). From the fast Fourier transformation (FFT) patterns (**Figure 1f, g**), both samples display clean reflection spots that can be indexed by the rocksalt structure with no diffuse scattering patterns surrounding the Bragg reflections, indicating no short-ranging ordering that is reported on other DRX system.[18] The electrochemistry of both samples is evaluated under the exactly same conditions (C/20, 4.8 - 1.5 V) (**Figure 1h**), therefore, the

variation is mostly related to the particle size, given no obvious difference in phase purity and local structure. Overall, LNTMOF sample produced at 700 ℃ exhibits the better performance, with an initial discharge capacity of 266 mAh g^{-1} and 200 mAh g^{-1} after 20 cycles. More importantly, the 700 ℃ sample displays a higher discharge capacity in the high voltage region, suggesting the kinetics of the corresponding redox reaction is also sensitive to the particle size of the DRX material. Given the optimal performance of the 700 ℃ sample, this material is used for the detailed characterization hereinafter.

Electroanalytical Characterization

The voltage profiles of the LNTMOF cathode indicate various redox processes perhaps participate in the electrochemistry at different voltages. Here, a series of electrochemical tests are designed to further understand the interplay among these redox reactions. Note all the cells were subjected to a full activation cycle between 4.8 and 1.5 V before the galvanostatic tests at varied charge and discharge cutoff voltages.[7, 38]

Increasing the upper charge cutoff voltage provides information on the cathodic reaction evolution during discharge (**Figure 2a, c**). The first feature is the emerging high-voltage cathodic peak that starts at 3.8 V charge and completes at 4.4 V charge. The second feature is the low-voltage cathodic peak around 2.0 V, the intensity of which remains same at the charge cutoff voltage below 3.5 V before a continuous increase until 4.8 V charge. Similarly, increasing the charge cutoff voltage beyond 3.8 V also leads to a continuously increased cathodic peak around 3.0 V. So both the 2.0 and 3.0 V cathodic peaks are correlated with the high-voltage redox process.

Similar findings on the evolution of the anodic peaks are obtained on the third charge to 4.8 V after gradually decreasing the cutoff voltage during the second discharge (**Figure 2b, d**). The 3.9 V anodic peak is characterized by a large increase with discharge voltage decreasing from 4.0 V to 2.8 V, paired with the 3.8 V cathodic peak, as well as a small increase from 2.5 to 1.8 V, where the 2.0 V cathodic peak evolves, suggesting the 2.0 V reduction reaction is somehow associated with the 3.9 V cathodic reaction. Meanwhile, the correlation between the 2.2 V anodic peak and 2.0 V cathodic peak is clearly shown. However, additional redox reactions must contribute to the 2.0 V cathodic peak based on their evolution behaviors at different charge cutoff voltages (**Figure 2c**). A significant increase in the 4.4 V anodic peak is observed when decreasing the discharge cutoff voltage below 2.5 V. Again, this observation is consistent with that on the 2.0 V cathodic peak from the charge cutoff voltage study discussed above. In brief, these results reveal different redox pairs around 3.9/3.8 V and 2.2/2.0 V, but a strongly coupled anodic oxidation reaction above 4.0 V and cathodic reduction reactions below 2.5 V.

Correspondingly, the voltage hysteresis for different redox processes in LNTMOF are investigated by the galvanostatic intermittent titration technique (GITT) test. The GITT tests are performed on the second cycle after the full activation at 4.8 – 1.5 V during the first cycle. Note 4.15 V charge cutoff is selected to eliminate the high-voltage redox reactions. Cells are rested for 8 h after galvanostatic charge/discharge at C/20 for 1.5 h. Based on the open circuit voltage after resting, a larger difference in the equilibrium voltage between charge and discharge is observed in the lower-voltage region within the full voltage window of 4.8 – 1.5 V (**Figure 2e**). In contrast, when the cell is only charged to 4.15 V without the high-voltage redox processes, the voltage difference is significantly reduced (**Figure 2f**). However, in either case, the large

polarization is mainly observed on the reduction process during discharge. Clearly, the large voltage hysteresis in the Ni-based DRX clearly mainly lies in the low-voltage region (equilibrium voltage of ~2.45 V) and is largely triggered by the high-voltage redox reactions. This behavior is in sharp contrast with that in the Mn-based DRX, which is associated with the high-voltage redox reactions.[34]

Cationic Redox Processes and Associated Structural Evolution

The distinct redox processes have been revealed in the previous section, a number of *ex situ* electrodes were prepared for spectroscopic studies to probe the chemical state change during electrochemical cycling.[39] Bulk-sensitive Ni *L*-edge X-ray absorption spectroscopy (XAS) in the total fluorescence yield (TFY) mode are collected at designated states of charge (SOCs) during the first cycle (**Figure 3a**) as well as the second charge to examine the low-voltage anodic process (**Figure 3b**). Ni^{2+}, Ni^{3+}, and Ni^{4+} reference spectra are calculated in an octahedral crystal field with single impurity Anderson model based on atomic multiple theory.[40, 41] Clearly, Ni starts from 2+ at pristine state (dash lines in **Figure 3a**), when charged to 4.15 V, it is oxidized to 3+ along with the presence of Ni^{4+}. Further charging to 4.8 V results in no significant change in Ni *L*-edge XAS. During discharge, bulk Ni reduction mostly takes place between 4.8 and 2.6 V, but with some reduction till 1.5 V discharge. This explains the 3.9 V cathodic increase when discharged below 2.5 V in **Figure 2d**. During the second charge (**Figure 3b**), Ni oxidation occurs above 3.0 V, which is evidenced by the comparison between the 1.5 V discharge state (dash lines in **Figure 3b**) and the charged state. Note that, similar to other Ni-based cathodes[42-44], the Ni state is largely reduced on the surface of the LNTMOF material, as revealed by the Ni *L*-edge XAS in surface-sensitive total electron yield (TEY) mode (**Figure S3**). The strong signals

of the reduced surface Ni contribute to the TFY spectra, leading to less contrast among the Ni spectra compared with the references. Additional information regarding the chemical state of Ni can be further obtained from the pre-edge peaks of O *K*-edge XAS.[9, 33, 45] The characteristic pre-edge peak of $Ni^{3+/4+}$–O is located at 528.7 eV (**Figure S4**). It is noted that the 528.7 eV pre-edge peak still increases from 4.15 to 4.8 V and continuous decrease occurs till 1.5 V discharge, but exhibits little change before 3.0 V on the second charge. Combined Ni *L*-edge and O *K* pre-edge XAS results suggest the Ni oxidation reaction still occurs at high voltages till 4.8 V and reduction reaction continues till 1.5 V discharge.

The oxidation states of Ti and Mo are also characterized to understand the possible redox contribution. It has been found that Ti-*L* XAS is not very sensitive on its spectroscopic lineshape upon oxidation state, but the resonant inelastic X-ray scattering (RIXS) of Ti-*L* could detect a clear contrast if the Ti oxidation state changes, with an *d-d* excitation feature in the Ti^{3+} states but nothing for Ti^{4+} due to the d^0 configuration.[46] We therefore employ the Ti *L*-edge RIXS at the excitation energy of 458.6 eV to evaluate the Ti state. As shown in **Figure 3c** & **Figure S5**, no noticeable feature could be seen in the emission energy range of 455 – 458.6 eV, suggesting that the Ti maintains its d^0 (Ti^{4+}) state.[46] Therefore, Ti is electrochemically inactive during cycling. The evolution of Mo chemical state is probed by Mo L_3-edge XAS (**Figure 3d**). As expected, Mo is 6+ at pristine state, in accordance with MoO_3 reference compound. By comparing the energy of the rising edge, slight Mo reduction is observed from 3.2 V to 1.5 V discharge, which confirms the small Mo contribution to the low-voltage redox around 2.0 V.

Additionally, the Mo L_3-edge XAS spectra provide the local symmetry of Mo cation. For Mo^{6+} cation, Mo L_3-edge is characterized by the duplex feature. The energy splitting is an indication of

the coordination of Mo^{6+} 4*d*-orbitals, with the value in tetrahedral coordination (T_d) being smaller than that in the octahedral one (O_h).[47] The typical ranges of the energy splitting are 3.1 – 4.5 eV and 1.8 – 2.4 eV for octahedral- and tetrahedral-coordinated Mo^{6+}, respectively.[47-49] The large difference in the crystal field splitting between the octahedral and tetrahedral coordination provides a unique way to examine the Mo migration during the charge/discharge process. The associated split energy can be visualized by taking the second derivative of the intensity after smoothing the spectra with respect to the energy (**Figure 4**). Based on the split energy (**Figure 4a**), it can be seen that Mo is located on the octahedral site at pristine state with the large energy splitting between the two main peaks. Upon charging, a gradual decrease in the split energy is observed from 3.9 eV at pristine state to 3.0 eV after fully charged, suggesting the Mo cation migration from octahedral to tetrahedral site. On the second charge, Mo $T_d \rightarrow O_h$ migration is partially reversible compared to its pristine state (**Figure 4a**). The migration after the initial charge is mostly reversible when comparing the same SOCs on the first and second cycle (**Figure 4b**).

Overall, Ni is the major redox center, and the oxidation/reduction reactions mostly occur at high voltages (~3.8 V), with small Ni reduction occurs at low voltages. Mo contributes to a small reversible redox in the low-voltage region, while Ti^{4+} remains inactive throughout the cycling. Interestingly, Mo displays the $O_h \rightarrow T_d$ cation migration during initial charge, which becomes partially reversible in later cycling.

Anionic Oxygen Redox Process

The participation of the O redox reaction is investigated by the high-efficiency RIXS mapping.[50, 51] The fingerprint of the oxidized O feature (red arrows in **Figure 5a**) at the excitation and

emission energies of 531.0 and 523.5 eV, respectively, can be observed at the 4.8 V charged state. During discharge, the feature sustains and can still be seen at the 3.2 V discharged state. The O *K*-edge RIXS cut at the 531.0 eV excitation energy allows us to closely examine the evolution of this oxidized O feature (characteristic peak at 523.5 eV) at different SOCs (**Figure 5b, c**). The dash lines in **Figure 5b** and **Figure 5c** are the spectra at pristine and 1.5 V discharged states, respectively. It can be seen that the 523.5 eV peak at 4.15 V charge shows a negligible increase compared to the pristine state, followed by a significant enhancement upon further charging to 4.8 V. O reduction starts to take place during discharge, but still with a finite content of oxidized oxygen feature at 3.2 V discharge until it disappears around 2.6 V discharge. During the 2nd charge, the O oxidation reaction again takes place at high voltages above 4.3 V, but the intensity drops significantly in the 2nd cycle charged sample. According to the O *K*-edge RIXS results, the lattice O redox reaction decays pretty fast upon cycling, which takes place at high voltages during charging but relatively low voltages during discharging.

Discussion of Mo Cation Migration and Anionic O Redox

Despite the same structural family, Ni^{2+}-based DRX materials exhibit very different electrochemical behaviors from those of the Mn^{3+}-based DRXs, manifested by the significant voltage hysteresis in the low-voltage region (~2 V).[11, 33, 35, 52, 53] The combined electroanalytical and spectroscopic studies reveal the distinct redox processes and local structural evolution related to the Mo cation $O_h \rightarrow T_d$ migration.

In order to understand the Mo migration mechanism in LNTMOF ($Li_{1.15}Ni_{0.45}Ti_{0.3}Mo_{0.1}O_{1.85}F_{0.15}$), we synthesize a Mo-free DRX sample, $Li_{1.15}Ni_{0.35}Ti_{0.5}O_{1.85}F_{0.15}$ (LNTOF), with the Li and F content fixed but varied Ni and Ti content. We hypothesize the charge capacity is mostly

determined by the Li content as Ni and/or O oxidation could compensate the charge mechanism at the different portion.[54] Previous work shows that F mostly influences the high-voltage activity and inhibits oxygen gas release.[10, 22, 28, 55, 56] As expected, both LNTMOF and LNTOF exhibit a similar initial charge capacity (~300 mAh/g) (**Figure 6a**). Upon discharging, since LNTOF has less Ni compared to LNTMOF (0.35 vs. 0.45 per formula unit), less capacity originating from the Ni redox is obtained at the high-voltage plateau. However, a quite large difference is observed at the low-voltage plateau, where more capacity is obtained in LNTOF than LNTMOF. It is also found that the voltage curve in the medium-voltage region (3.2 – 2.2 V) has been shifted upwards significantly, which is consistent with the O *K*-edge RIXS results, indicating the oxygen reduction till ~2.6 V discharge in LNTMOF. Clearly, introducing Mo into LNTOF system increases the potential of oxygen reduction reaction. However, the O_2 gas evolution is also promoted by Mo based on the DEMS results, revealing O_2 gas release of 5.2 mmol/mol LNTOF, much less than 17.7 mmol/mol LNTMOF (**Figure 6d**). Accordingly, the Mo L_3-edge reveals the Mo cation migration from octahedral to tetrahedral site during the first charge. We note that cation migration was found to be coupled to the oxygen redox activities in Li-rich layered compounds[57], which could be the case here in LNTMOF material.

Upon cycling, the redox reactions at 2.0 V plateau in LNTMOF is more reversible compared to that in LNTOF, suggesting the different redox mechanism at low voltages that go beyond the O_2 gas evolution upon high-voltage charging. According to TM *L*-edge XAS, the low voltage region in LNTMOF is mainly dominated by Ni and Mo reduction. Less Ni in LNTOF system but comparable charge capacity suggests more O oxidation during charge. Given the less oxygen gas release from LNTOF, more O reduction reaction would occur during discharge, which leads to

more capacity decay in LNTOF system (especially around 2.0 V). It still remains critical to stabilize the oxygen redox in the Ni-based DRX materials. This work reveals the evidence of possible pathways to boost the energy efficiency by enhancing the oxygen reduction potential through the appropriate d^0 TM along besides the fluorination and surface protection.

Conclusions

We report the synthesis and electrochemistry of Li-excess cation disordered rocksalt of Ni^{2+}-Ti^{4+}-Mo^{6+} (LNTMOF). Regardless of the calcination temperature, this material exhibits no short-range ordering. We probe the complex redox reactions of incomplete $Ni^{2+/4+}$ and O accompanied by oxygen gas release at high-voltage charge and small Mo reduction at low-voltage discharge. Interestingly, Mo *L*-edge XAS spectra reveal the Mo cation migration from octahedral to tetrahedral sites that seems to be coupled with the oxygen redox and promotes the O reduction potential. This study demonstrates the interplay among TM cation and O anion as well as the role of inactive d^0 Mo in Ni-based DRX cathodes, which warrant the necessity of such comprehensive understanding for the further enhancements of this new family cathode materials.

EXPERIMENTAL PROCEDURES

Resource Availability

Lead Contact

Further information and requests for resources should be directed to and will be fulfilled by the Lead Contact, Wei Tong (weitong@lbl.gov).

Synthesis

LNTMOF compound was synthesized via a solid-state reaction. Stoichiometric amounts of Li_2CO_3, $NiCO_3$, TiO_2, MoO_2, and LiF precursors were thoroughly mixed by high-energy ball milling for 3 h, then calcined at 700 or 800 °C for 10 h in air. The synthesized powders were collected and stored in an Ar-filled glovebox to prevent exposure to air and moisture. LNTOF control sample was prepared using a similar method at a calcination temperature of 700 °C for 10 h.

Physical Characterization

XRD patterns were collected on a Bruker D2-Phaser with Cu Kα radiation (λ = 1.54178 Å). The structural information was obtained through the conventional Rietveld refinement analysis using general structure analysis system package with the graphical user interface (EXPGUI).[58] STEM imaging and energy-dispersive X-ray spectroscopy (EDS) mapping are performed on an aberration-corrected JEOL JEM-ARM200CF with the operation voltage of 200 kV.

Electrochemical Characterization

The as-produced LNTMOF powder was first mixed with carbon black at a weight ratio of 70:20 to increase the electronic conductivity of the composite electrode, then mixed with polyvinylidene fluoride (PVdF, 6 wt%) dissolved into N-methylpyrrolidone solvent in an Ar-filled glovebox to form a uniform slurry (LNTMOF: acetylene black: PVdF = 70: 20: 10 in weight). The slurry was casted on an aluminum foil (20 μm thickness) using a doctor blade and dried at 120 ºC under vacuum overnight. The punched electrode was assembled inside a 2032-type coin cell along with Li metal, separator (Celgard 2400), and electrolyte (1 M $LiPF_6$ in 1:2 w/ w ethylene carbonate–diethyl carbonate) in an Ar-filled glovebox. The mass loading of

LNTMOF material was ~2.5 mg cm^{-2}. 1C capacity was defined as 295.2 mAh g^{-1} (theoretical capacity of 1 Li^+ from LNTMOF).

XAS and RIXS

Ni *L*-edge XAS, Ti *L*-edge, and O *K*-edge RIXS were carried out at ultrahigh efficiency iRIXS endstation at Beamline 8.0.1 at the Advanced Light Sources (ALS).[59] Mo *L*-edge XAS was performed at Beamline 5.3.1 at the ALS. Ti *L*-edge XAS measurements were performed on beamline 10-1 at Stanford Synchrotron Radiation Lightsource. Mo *L*-edge XAS spectra were measured under constant He flow. Mo *L*-edge XAS data points were smoothed using the Adjacent-Averaging method with 5 points of window. For RIXS experiments, the cycled LNTMOF electrodes were immediately removed from the coin cells inside an Ar-filled glovebox once the cells reached the designated states of charge to minimize the side reactions. The harvested electrodes were then rinsed by dimethyl carbonate solvent to remove surface species. All the dried electrodes were sealed in a home-made sample transfer kit inside an Ar-filled glove box, then transferred into the experimental vacuum chamber to avoid any air/moisture exposure. The resolution of the excitation energy is about 0.2 eV and the emission energy about 0.35 eV. An excitation energy step size of 0.2 eV was used for all maps. All technical details on RIXS geometry and spectrometer setups can be found in our previous report.[59] All the spectra were normalized to the beam flux measured by the upstream gold mesh, and RIXS spectra were also normalized to the collection time for each individual cut.

DEMS

CO_2 and O_2 gas evolution was measured using DEMS. The carbon-processed LNTMOF powder was mixed with polytetrafluoroethylene (PTFE) binder at a weight ratio of 70:20:10 inside an

Ar-filled glovebox. A piece of electrode film was prepared by pressing the mixed powder onto a stainless-steel mesh current collector and sealed in a customized Swagelok type cell with Li metal, one sheet of Whatman quartz microfiber filter paper on the anode side and one sheet of Celgard 2500 on the cathode side, and electrolyte (1M $LiPF_6$ in 1:1 vol/vol ethylene carbonate-diethyl carbonate). The hermetically sealed cell was appropriately attached to the DEMS apparatus to avoid air exposure. The DEMS cell was initially rested at the open circuit voltage for 2 h before applying a current at C/10 (4.8 – 1.5 V) for galvanostatic charge/discharge using a BioLogic SP-300 potentiostat. The detailed procedures for the gas measurement and analysis are described in a previous report.[60]

ACKNOWLEDGEMENTS

This work is supported by the Assistant Secretary for Energy Efficiency and Renewable Energy, Office of Vehicle Technologies of the U.S. Department of Energy under Contract No. DE-AC02-05CH11231. Use of the Advanced Light Source is supported by the Office of Science, Office of Basic Energy Sciences, of the US Department of Energy under contract No. DE-AC02-05CH11231. Use of resources at the Molecular Foundry was supported by the Office of Science, Office of Basic Energy Sciences, of the U.S. Department of Energy under Contract No. DE-AC02-05CH11231. Use of the Stanford Synchrotron Radiation Lightsource, SLAC National Accelerator Laboratory, is supported by the U.S. Department of Energy, Office of Science, Office of Basic Energy Sciences under Contract No. DE-AC02-76SF00515.

AUTHOR CONTRIBUTIONS

W.T. and Y.Y. designed the experiments; Y.Y. synthesized, characterized the materials and analyzed the data with W.T. and N.L; Y.Y. performed Ti-*L* XAS, Y.H., Q.L., J.F., and W.Y.

performed spectroscopic experiments and analysis, T.-Z.Y. and B.D.M. measured and analyzed gas evolution; L.Z. and C.W. carried out the TEM analysis. Y.Y. and W.T. wrote the manuscript with the inputs from all authors.

DECLARATION OF INTERESTS

The authors declare no competing interests.

REFERENCES

[1] J. Desilvestro and O. Haas, *J. Electrochem. Soc.*, **1990**, *137*, 5C-22C.

[2] J.-M. Tarascon and M. Armand, *Nature*, **2001**, *414*, 359-367.

[3] M. S. Whittingham, *Chem. Rev.*, **2004**, *104*, 4271-4302.

[4] J. Lee, A. Urban, X. Li, D. Su, G. Hautier and G. Ceder, *Science*, **2014**, *343*, 519-522.

[5] A. Urban, J. Lee and G. Ceder, *Adv. Energy Mater.*, **2014**, *4*, 1400478.

[6] R. Clément, Z. Lun and G. Ceder, *Energy Environ. Sci.*, **2020**, *13*, 345-373.

[7] S. L. Glazier, J. Li, J. Zhou, T. Bond and J. Dahn, *Chem. Mater.*, **2015**, *27*, 7751-7756.

[8] A. Kitajou, K. Tanaka, H. Miki, H. Koga, T. Okajima and S. Okada, *Electrochemistry*, **2016**, *84*, 597-600.

[9] N. Yabuuchi, M. Takeuchi, M. Nakayama, H. Shiiba, M. Ogawa, K. Nakayama, T. Ohta, D. Endo, T. Ozaki and T. Inamasu, *PNAS*, **2015**, *112*, 7650-7655.

[10] J. Lee, D.-H. Seo, M. Balasubramanian, N. Twu, X. Li and G. Ceder, *Energy Environ. Sci.*, **2015**, *8*, 3255-3265.

[11] R. Wang, X. Li, L. Liu, J. Lee, D.-H. Seo, S.-H. Bo, A. Urban and G. Ceder, *Electrochem. Commun.*, **2015**, *60*, 70-73.

[12] N. Yabuuchi, M. Nakayama, M. Takeuchi, S. Komaba, Y. Hashimoto, T. Mukai, H. Shiiba, K. Sato, Y. Kobayashi and A. Nakao, *Nat. Commun.*, **2016**, *7*, 13814.

[13] T. Matsuhara, Y. Tsuchiya, K. Yamanaka, K. Mitsuhara, T. Ohta and N. Yabuuchi, *Electrochemistry*, **2016**, *84*, 797-801.

[14] N. Yabuuchi, M. Takeuchi, S. Komaba, S. Ichikawa, T. Ozaki and T. Inamasu, *Chem. Commun.*, **2016**, *52*, 2051-2054.

[15] A. Urban, I. Matts, A. Abdellahi and G. Ceder, *Adv. Energy Mater.*, **2016**, *6*, 1600488.

[16] X. Wang, Y. Huang, D. Ji, F. Omenya, K. Karki, S. Sallis, L. F. Piper, K. M. Wiaderek, K. W. Chapman and N. A. Chernova, *J. Electrochem. Soc.*, **2017**, *164*, A1552-A1558.

[17] J. Lee, D. A. Kitchaev, D.-H. Kwon, C.-W. Lee, J. K. Papp, Y.-S. Liu, Z. Lun, R. J. Clément, T. Shi, B. D. McCloskey, J. Guo, M. Balasubramanian and G. Ceder, *Nature*, **2018**, *556*, 185-190.

[18] H. Ji, A. Urban, D. A. Kitchaev, D.-H. Kwon, N. Artrith, C. Ophus, W. Huang, Z. Cai, T. Shi, J. C. Kim, H. Kim and G. Ceder, *Nat. Commun.*, **2019**, *10*, 592.

[19] M. Luo, S. Zheng, J. Wu, K. Zhou, W. Zuo, M. Feng, H. He, R. Liu, J. Zhu, G. Zhao, S. Chen, W. Yang, Z. Peng, Q. Wu and Y. Yang, *J. Mater. Chem. A*, **2020**, *8*, 5115-5127.

[20] R. Chen, S. Ren, M. Yavuz, A. A. Guda, V. Shapovalov, R. Witter, M. Fichtner and H. Hahn, *Phys. Chem. Chem. Phys.*, **2015**, *17*, 17288-17295.

[21] W. D. Richards, S. T. Dacek, D. A. Kitchaev and G. Ceder, *Adv. Energy Mater.*, **2018**, *8*, 1701533.

[22] Z. Lun, B. Ouyang, D. A. Kitchaev, R. J. Clément, J. K. Papp, M. Balasubramanian, Y. Tian, T. Lei, T. Shi, B. D. McCloskey, J. Lee and G. Ceder, *Adv. Energy Mater.*, **2018**, *8*, 1802959.

[23] J. Xu, S. Renfrew, M. A. Marcus, M. Sun, B. D. McCloskey and W. Tong, *J. Phys. Chem. C*, **2017**, *121*, 11100-11107.

[24] J. Kim, H. Lee, H. Cha, M. Yoon, M. Park and J. Cho, *Adv. Energy Mater.*, **2018**, *8*, 1702028.

[25] R. Clément, Z. Lun and G. Ceder, *Energy Environ. Sci.*, **2020**.

[26] Q. Jacquet, A. Iadecola, M. Saubanère, H. Li, E. J. Berg, G. Rousse, J. Cabana, M.-L. Doublet and J.-M. Tarascon, *J. Am. Chem. Soc.*, **2019**, *141*, 11452-11464.

[27] M. A. Cambaz, A. Urban, S. A. Pervez, H. Geßwein, A. Schiele, A. A. Guda, A. L. Bugaev, A. Mazilkin, T. Diemant, R. J. Behm, T. Brezesinski and M. Fichtner, *Chem. Mater.*, **2020**, *32*, 3447-3461.

[28] J. Lee, J. K. Papp, R. J. Clément, S. Sallis, D.-H. Kwon, T. Shi, W. Yang, B. D. McCloskey and G. Ceder, *Nat. Commun.*, **2017**, *8*, 981.

[29] M. A. Cambaz, B. P. Vinayan, H. Geßwein, A. Schiele, A. Sarapulova, T. Diemant, A. Mazilkin, T. Brezesinski, R. J. Behm and H. Ehrenberg, *Chem. Mater.*, **2019**, *31*, 4330-4340.

[30] Z. Yu, X. Qu, A. Dou, M. Su, Y. Liu and F. Wu, *ACS Appl. Mater. Interfaces*, **2019**, *11*, 35777-35787.

[31] H. Ji, D. A. Kitchaev, Z. Lun, H. Kim, E. Foley, D.-H. Kwon, Y. Tian, M. Balasubramanian, M. Bianchini, Z. Cai, R. J. Clément, J. C. Kim and G. Ceder, *Chem. Mater.*, **2019**, *31*, 2431-2442.

[32] E. Zhao, L. He, B. Wang, X. Li, J. Zhang, Y. Wu, J. Chen, S. Zhang, T. Liang and Y. Chen, *Energy Storage Mater.*, **2019**, *16*, 354-363.

[33] W. H. Kan, D. Chen, J. K. Papp, A. K. Shukla, A. Huq, C. M. Brown, B. D. McCloskey and G. Chen, *Chem. Mater.*, **2018**, *30*, 1655-1666.

[34] Y. Yue, N. Li, L. Li, E. E. Foley, Y. Fu, V. S. Battaglia, R. J. Clément, C. Wang and W. Tong, *Chem. Mater.*, **2020**, *32*, 4490-4498.

[35] B. Ouyang, N. Artrith, Z. Lun, Z. Jadidi, D. A. Kitchaev, H. Ji, A. Urban and G. Ceder, *Adv. Energy Mater.*, **2020**, 1903240.

[36] A. Urban, A. Abdellahi, S. Dacek, N. Artrith and G. Ceder, *Phys. Rev. Lett.*, **2017**, *119*, 176402.

[37] J. Xu, G. Babu, K. Kato, F. C. R. Hernández, A. B. Puthirath, A. Britz, D. Nordlund, S. Sainio, U. Bergmann and P. M. Ajayan, *Solid State Ionics*, **2020**, *345*, 115172.

[38] G. Assat, D. Foix, C. Delacourt, A. Iadecola, R. Dedryvère and J.-M. Tarascon, *Nat. Commun.*, **2017**, *8*, 2219.

[39] J. Wu, Y. Yang and W. Yang, *Dalton Trans.*, **2020**, *49*, 13519-13527.

[40] R. Qiao, J. Liu, K. Kourtakis, M. G. Roelofs, D. L. Peterson, J. P. Duff, D. T. Deibler, L. A. Wray and W. Yang, *J. Power Sources*, **2017**, *360*, 294-300.

[41] E. Zhao, Q. Li, F. Meng, J. Liu, J. Wang, L. He, Z. Jiang, Q. Zhang, X. Yu, L. Gu, W. Yang, H. Li, F. Wang and X. Huang, *Angew. Chem. Int. Edit.*, **2019**, *58*, 4323-4327.

[42] J. Xu, E. Hu, D. Nordlund, A. Mehta, S. N. Ehrlich, X.-Q. Yang and W. Tong, *ACS Appl. Mater. Interfaces*, **2016**, *8*, 31677-31683.

[43] J. Xu, F. Lin, D. Nordlund, E. J. Crumlin, F. Wang, J. Bai, M. M. Doeff and W. Tong, *Chem. Commun.*, **2016**, *52*, 4239-4242.

[44] S. Zheng, D. Liu, L. Tao, X. Fan, K. Liu, G. Liang, A. Dou, M. Su, Y. Liu and D. Chu, *J. Alloy. Compd.*, **2019**, *773*, 1-10.

[45] S. Roychoudhury, R. Qiao, Z. Zhuo, Q. Li, Y. Lyu, J. H. Kim, J. Liu, E. Lee, B. J. Polzin and J. Guo, *Energy Environ. Mater.*, **2020**, *3*, doi: 10.1002/EEM1002.12119.

[46] A. Augustsson, A. Henningsson, S. M. Butorin, H. Siegbahn, J. Nordgren and J.-H. Guo, *J. Chem. Phys.*, **2003**, *119*, 3983-3987.

[47] S. R. Bare, G. E. Mitchell, J. J. Maj, G. E. Vrieland and J. L. Gland, *J. Phys. Chem.*, **1993**, *97*, 6048-6053.

[48] G. George, W. Cleland Jr, J. Enemark, B. Smith, C. Kipke, S. Roberts and S. P. Cramer, *J. Am. Chem. Soc.*, **1990**, *112*, 2541-2548.

[49] E. Lede, F. Requejo, B. Pawelec and J. Fierro, *J. Phys. Chem. B*, **2002**, *106*, 7824-7831.

[50] W. Yang and T. P. Devereaux, *J. Power Sources*, **2018**, *389*, 188-197.

[51] K. Dai, J. Wu, Z. Zhuo, Q. Li, S. Sallis, J. Mao, G. Ai, C. Sun, Z. Li, W. E. Gent, W. C. Chueh, Y.-d. Chuang, R. Zeng, Z.-x. Shen, F. Pan, S. Yan, L. F. J. Piper, Z. Hussain, G. Liu and W. Yang, *Joule*, **2019**, *3*, 518-541.

[52] B. Huang, R. Wang, Y. Gong, B. He and H. Wang, *Frontiers in chemistry*, **2019**, *7*, 107.

[53] M. A. Jones, P. J. Reeves, M. J. Cliffe, S. E. Dutton and C. P. Grey, *Chem. Commun.*, **2019**, *55*, 9027-9030.

[54] Z. Lun, B. Ouyang, Z. Cai, R. J. Clément, D.-H. Kwon, J. Huang, J. K. Papp, M. Balasubramanian, Y. Tian, B. D. McCloskey, H. Ji, H. Kim, D. Kitchaev and G. Ceder, *Chem*, **2020**, *6*, 153-168.

[55] M. J. Crafton, Y. Yue, T.-Y. Huang, W. Tong and B. D. McCloskey, *Adv. Energy Mater.*, **2020**, *10*, 2001500.

[56] K. Zhou, S. Zheng, F. Ren, J. Wu, H. Liu, M. Luo, X. Liu, Y. Xiang, C. Zhang and W. Yang, *Energy Storage Mater.*, **2020**, *32*, 234-243.

[57] W. E. Gent, K. Lim, Y. Liang, Q. Li, T. Barnes, S.-J. Ahn, K. H. Stone, M. McIntire, J. Hong, J. H. Song, Y. Li, A. Mehta, S. Ermon, T. Tyliszczak, D. Kilcoyne, D. Vine, J.-H. Park, S.-K. Doo, M. F. Toney, W. Yang, D. Prendergast and W. C. Chueh, *Nat. Commun.*, **2017**, *8*, 2091.

[58] B. H. Toby, *J. Appl. Crystallogr.*, **2001**, *34*, 210-213.

[59] R. Qiao, Q. Li, Z. Zhuo, S. Sallis, O. Fuchs, M. Blum, L. Weinhardt, C. Heske, J. Pepper, M. Jones, A. Brown, A. Spucces, K. Chow, B. Smith, P.-A. Glans, Y. Chen, S. Yan, F. Pan, L. F. J. Piper, J. Denlinger, J. Guo, Z. Hussain, Y.-D. Chuang and W. Yang, *Rev. Sci. Instrum.*, **2017**, *88*, 033106.

[60] B. D. McCloskey, D. S. Bethune, R. M. Shelby, G. Girishkumar and A. C. Luntz, *J. Phys. Chem. Lett.*, **2011**, *2*, 1161-1166.

Supplementary Information

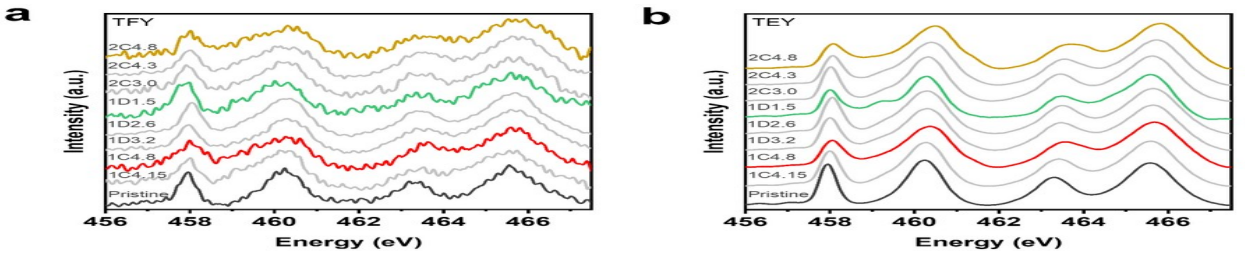

Figure S5. Ti L-edge XAS spectra of LNTMOF cathode during electrochemical cycling in (a) bulk-sensitive TFY and (b) surface-sensitive TEY modes.